Supplementary Information

SUPPLEMENTARY FIGURES

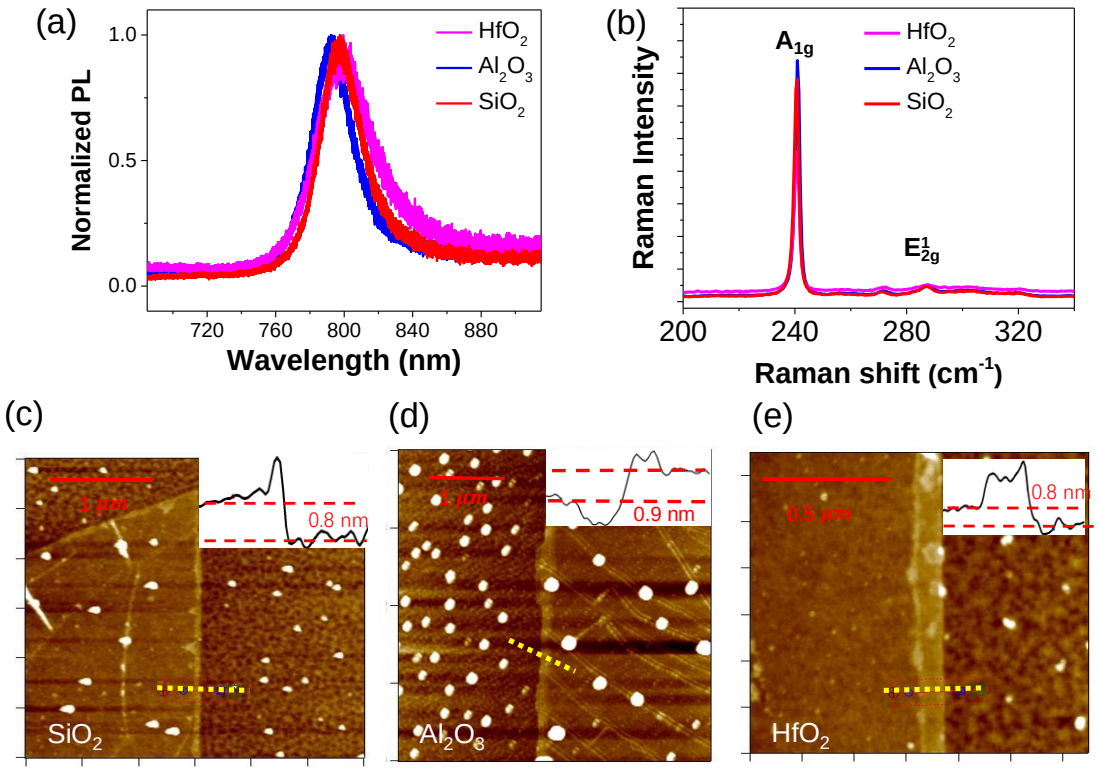

Supplementary Figure 1 (a) Normalized PL spectra; (b) normalized Raman spectra of $MoSe_2$ samples on different substrates; and the AFM images of $MoSe_2$ on (c) SiO_2, (d) Al_2O_3, and (e) HfO_2, where the insets show the cross-section profiles of the yellow dashed lines.

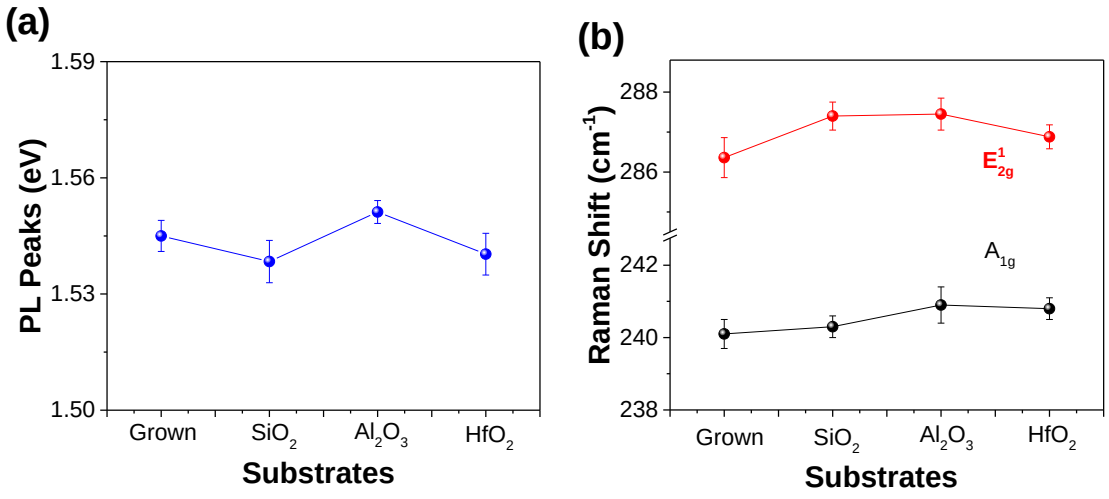

Supplementary Figure 2 (a) PL peak positions and (b) Raman modes' peak positions of monolayer

$MoSe_2$ on different substrates. The error bars represent one standard deviation from repeated experiments.

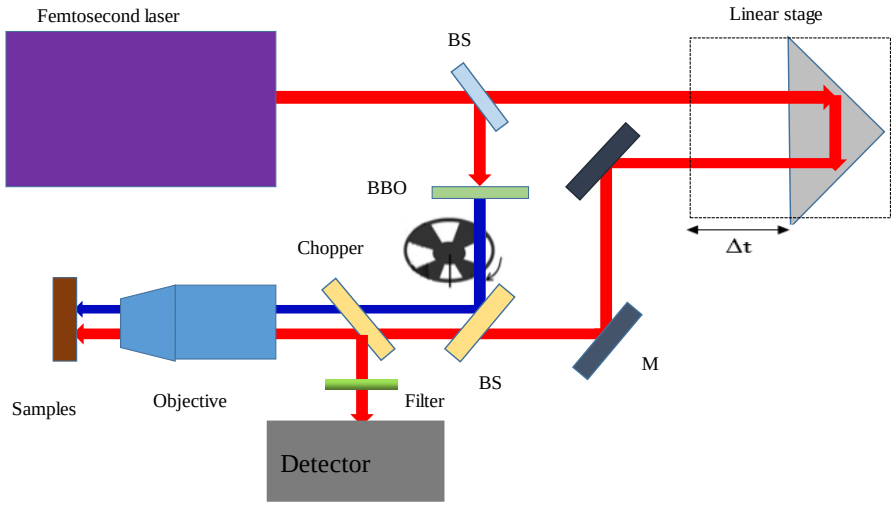

Supplementary Figure 3 Schematic illustration of the pump-probe setup. BS: beam splitter; BBO: Beta barium borate.

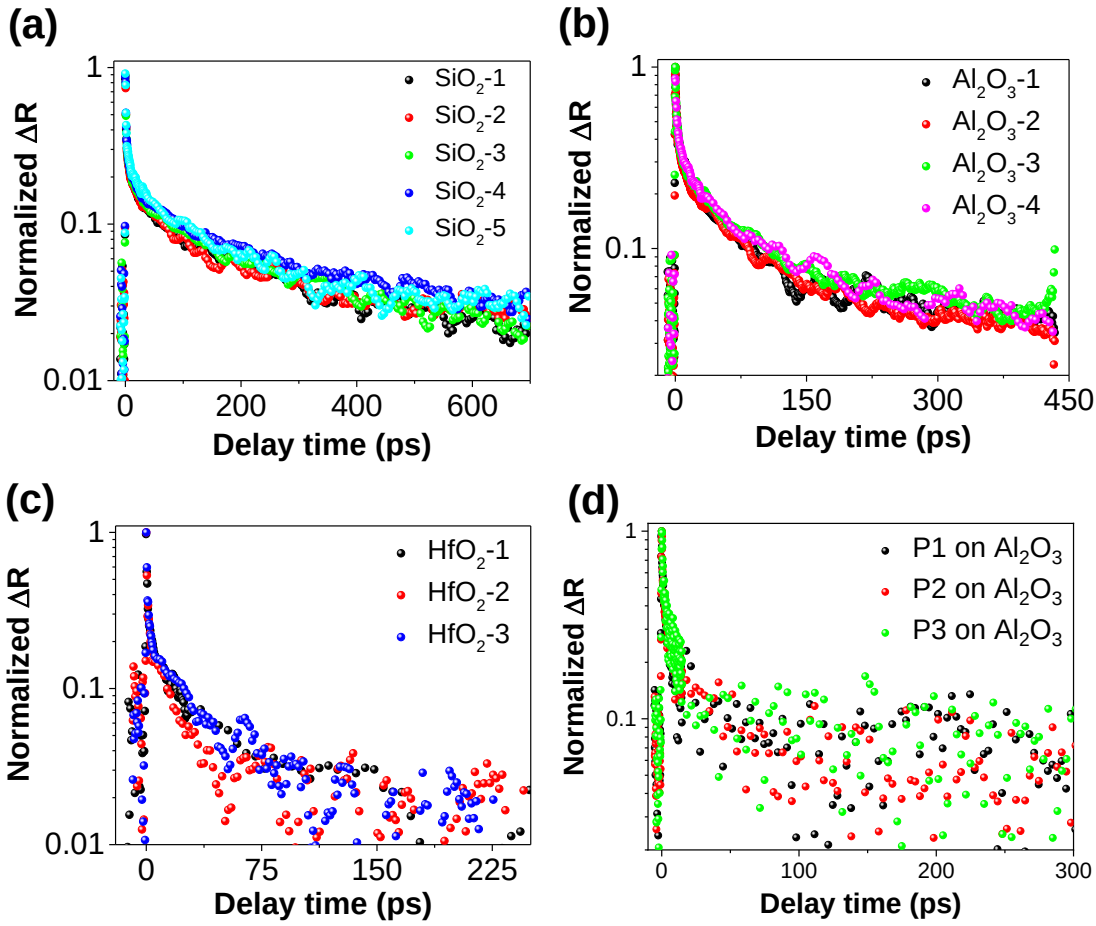

Supplementary Figure 4 Normalized transient reflectance curves of different flakes of monolayer

$MoSe_2$ on (a) SiO_2, (b) Al_2O_3, (c) HfO_2; (d) normalized dynamic curves of different points from the same $MoSe_2$ flake on Al_2O_3. The curves indicate that compared with the influence from substrates, the difference introduced in growth and transfer process can be negligible.

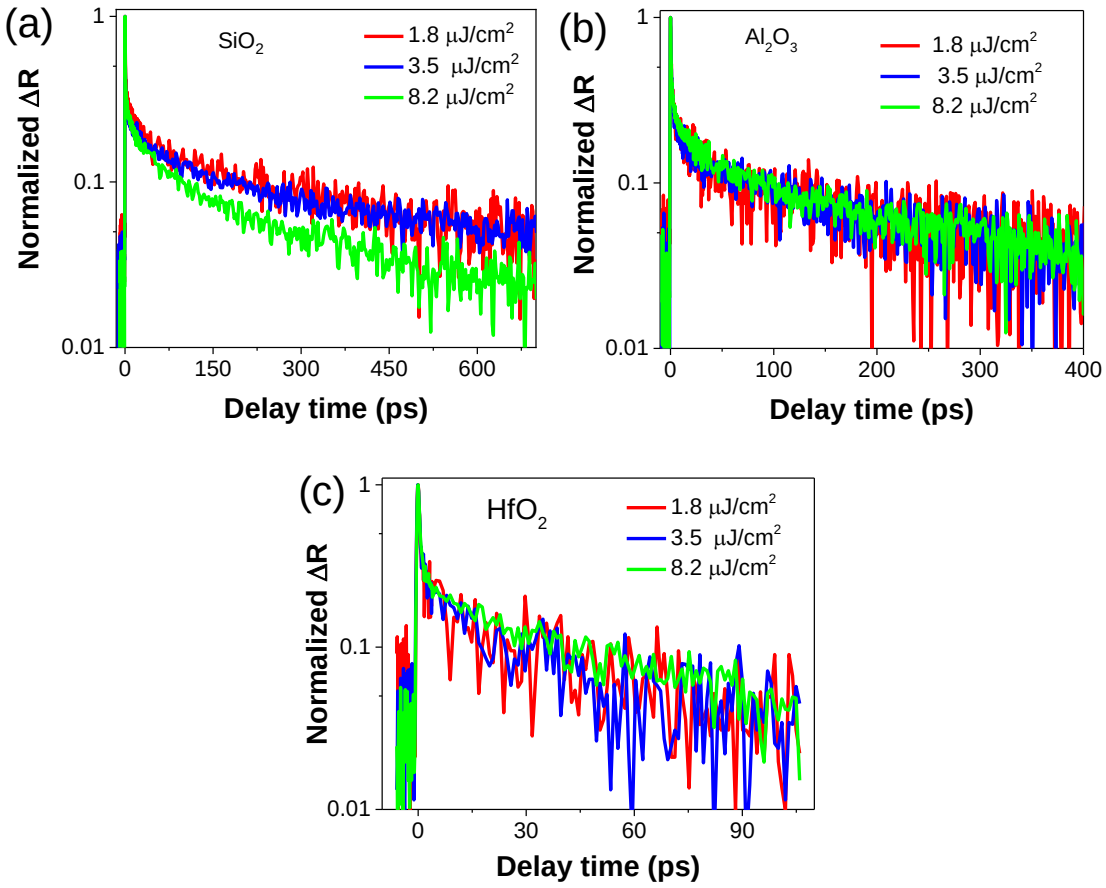

Supplementary Figure 5 The transient reflectance signals of monolayer $MoSe_2$ on different substrates: (a) SiO_2; (b) Al_2O_3, (c) HfO_2, under varying pump fluences. The well overlapped curves suggest there is no major effect from the pump fluence or exciton densities.

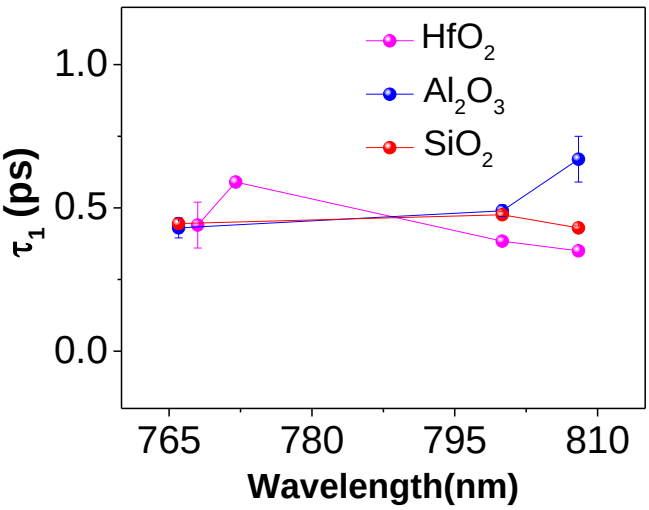

Supplementary Figure 6 The first relaxation time τ_1 of monolayer $MoSe_2$ on different substrates as a function of probe wavelengths. The solid lines are guide for eyes. The error bars represent one standard deviation from repeated experiments.

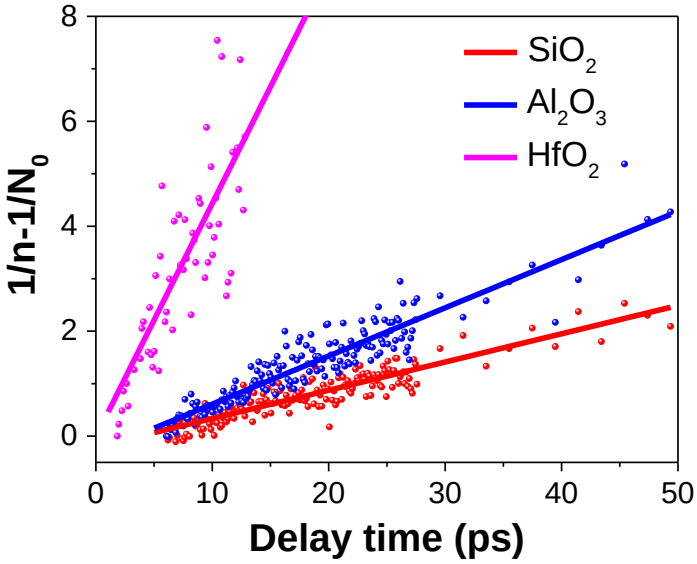

Supplementary Figure 7 ($1/n$-$1/N_0$) of monolayer $MoSe_2$ on different substrates. Dots are experimental data and lines are linear fitting based on EEA.

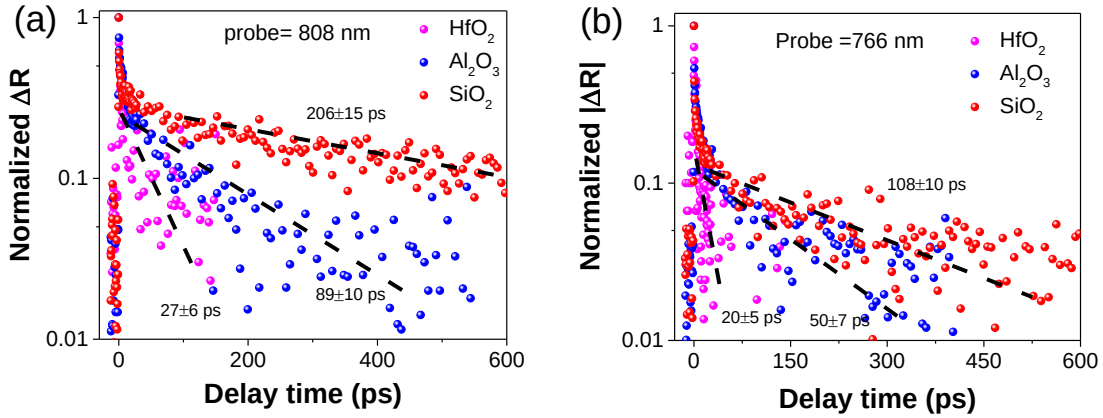

Supplementary Figure 8 Normalized dynamic signals of monolayer $MoSe_2$ on three different substrates when the probe wavelength is (a) 808 nm and (b) 766 nm.

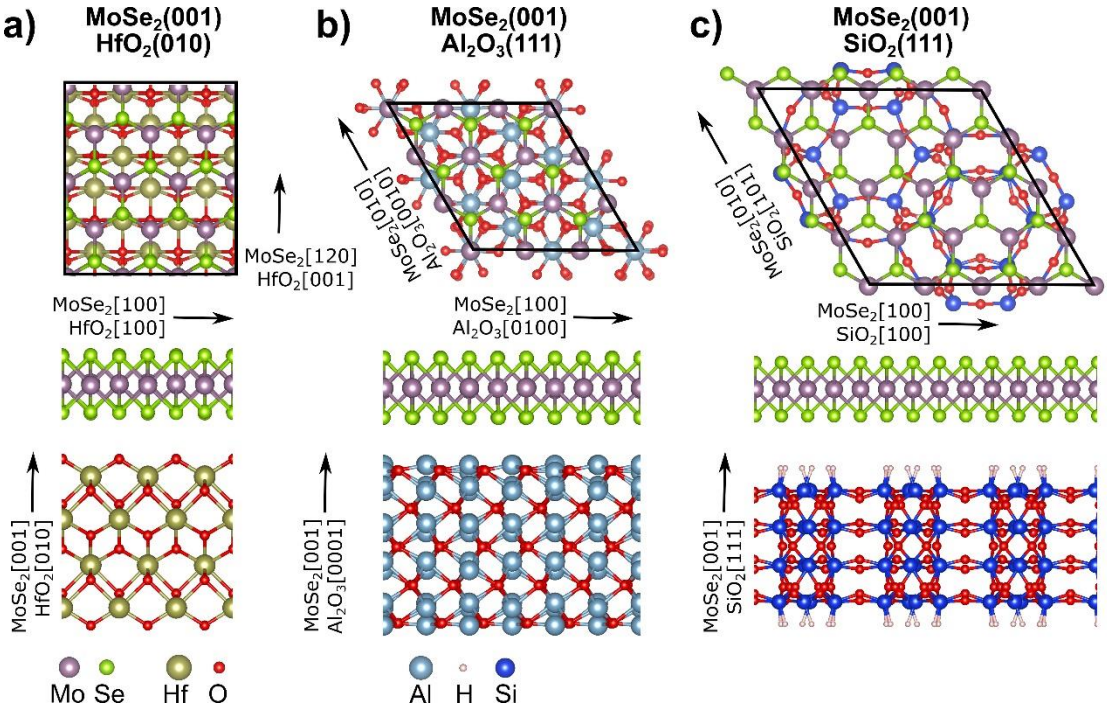

Supplementary Figure 9 The top and side views of (a) $HfO_2(010)(3\times3)||MoSe_2(001)(3\times2\sqrt{3})$, (b) $Al_2O_3(111)(2\times2)||$ $MoSe_2(001)(3\times3)$ and (c) $SiO_2(111)(1\times1)||MoSe_2(001)$ (4×4).

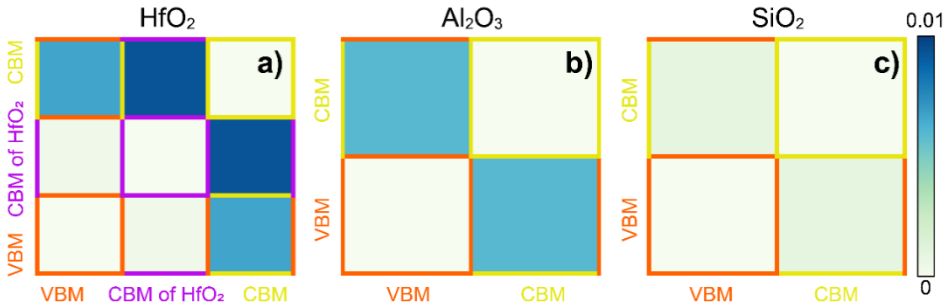

Supplementary Figure 10 (a-c) The NAC elements between different electronic states in $MoSe_2$ on HfO_2, Al_2O_3, and SiO_2 substrates.

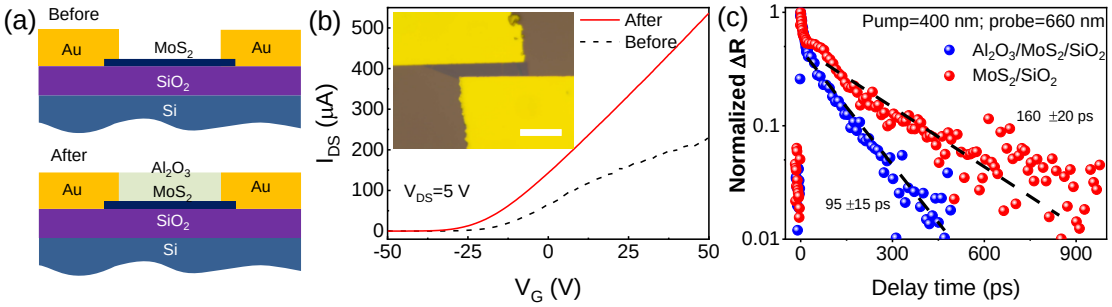

Supplementary Figure 11 (a) Schematic illustration of a monolayer MoS_2 field-effect transistor device before and after Al_2O_3 encapsulation. The Al_2O_3 layer is ~5 nm thick and deposited by ALD (not drawn to proportion). (b) Source-drain current I_{DS} as a function of the back-gate voltage V_G. The charge mobility inferred before and after Al_2O_3 encapsulation are 13.3 $cm^2V^{-1}S^{-1}$ and 23.0 $cm^2V^{-1}S^{-1}$, respectively. Inset shows the optical micrograph of the device, scale bar is 20 μm. (c) Normalized transient reflectance signal before and after Al_2O_3 encapsulation (pump=400 nm, probe=660 nm). The relaxation lifetimes are found to be 160±20 ps and 95±15 ps, respectively.

SUPPLEMENTARY NOTES 1: Exciton formation process

The first relaxation process stays almost constant for all samples (~400-500 fs), as shown in Supplementary Figure 6. In general, such fast process may have two different types of origins: either rapid loss of photocarriers, or evolution of photocarriers species. Firstly, the identical initial relaxation processes of samples on Al_2O_3 within first 5 ps at different pump intensities shows no obvious dependence on pump power. Furthermore, as the pump photon energy is much larger than the bandgap of $MoSe_2$, free carriers are expected to be generated immediately following photoexcitation. We extracted the ratio between the transient reflectance at time zero and at delayed time 3 ps. The calculated ratios of the three samples all exceed 2, confirming the existence of free carriers, since free carriers are more efficient in inducing transient reflection than excitons.[1] Thus we attribute this sub-picosecond decay to the intrinsic process of exciton formation, which has been proved both theoretically and experimentally.[1-4]

SUPPLEMENTARY NOTES 2: Rate equation including EEA process

We attribute the second relaxation component to some inter-exciton interaction induced process, such as exciton-exciton annihilation (EEA). To quantitatively evaluate EEA rate from the measured dynamic curves, the decay of exciton density n is described by: $\frac{dn}{dt} = -\frac{n}{\tau} - \gamma n^2$ where τ is the lifetime of exciton and γ is the EEA rate constant. One could attempt to analyze experimental data shown in Fig. 2(a) by the solution of the above equation. However, EEA is only significant in early time after photoexcitation when density of exciton is relatively high, thus we focus on the experimental data before 50 ps and ignore other process occurring on longer time scales.[5-7] The solution of the above equation can be simplified to: $\frac{1}{n} - \frac{1}{N_0} = \gamma t$ where N_0 is the

initial density of excitons. As illuminated in Supplementary Figure 7, $(1/n - 1/N_0)$ is proportional to delay time and EEA rate γ can be inferred from the linear fitting. EEA rate shows a variance for monolayer $MoSe_2$ on various substrates, from 0.0538 cm^2/s on SiO_2 to 0.44 cm^2/s on HfO_2. According to previous reports, EEA rate of TMDs is quite sensitive to surrounding environment. For example, encapsulation of TMDs by thin hBN films can lead to a suppression of EEA rate.[8]

SUPPLEMENTARY NOTES 3: Dielectric screening effect from substrates

Due to the atomic thickness of monolayer TMDs, the Coulombic interaction between electrons and holes in such systems is much stronger than that in bulk, leading to several superior properties. Since Coulomb interaction in low-dimensional systems is predicted to be strongly coupled with the dielectric properties of the surrounding environment, properties of monolayer TMDs, such as carrier mobility and binding energy, should be highly susceptible to the dielectric environment. Moreover, the strength of dielectric screening has been found to be directly proportional to the dielectric constant of the surrounding environment, where higher dielectric constant can induce stronger screening effect.[9,10] For example, with the increase of environmental dielectric constant, the binding energy of excitons in monolayer MoS_2 has been reported to reduce.[11]

Despite the common existence of such screening effect, experimental and theoretical analysis can help to rule it out as a dominant role in determining the non-radiative lifetime of excitons. Firstly, it has been found that the dielectric screening effect from high-k substrates could suppress the scattering by Coulomb impurities and traps and increase carrier mobility of TMDs. If such effect dominates the photocarrier dynamics in our investigation, TMDs on substrates with higher dielectric constants (for example, HfO_2) should demonstrate longer carrier lifetimes, which contradicts with

our observation.

Secondly, it is known that the substrate-induced screening could alter the exciton configuration in monolayer TMDs. In general, bandgap renormalization and binding energy reduction could happen at the same time. Although these two effects can partially cancel each other, the optical bandgap always changes to some extent.[11,12] For example, Lin et al. found that the change in dielectric environment could lead to the blue shift (~40 meV) of PL peaks.[11] In this study, as shown by Supplementary Figure 2, monolayer $MoSe_2$ on the three different substrates demonstrated constant PL peak position, whose variance was less than 10 meV. This suggests that the influence of dielectric screening on excitonic binding states may not be significant here.

In addition, the change of excitonic binding states normally affects the radiative channel and the exciton decay time can be estimated as:

$$\tau_{rad}^{0} = \frac{\hbar\varepsilon}{2k_0}\left(\frac{E_{X^0}}{e\hbar\nu}\right)^2 (a_B^{2D})^2$$

where $k_0 = E_{X^0}\sqrt{\varepsilon}/\hbar c$ is the light wave-vector in the sample (c is the speed of light, ε is the dielectric constant, E_{X^0} is the exciton transition energy) and ν is the Kane velocity related to the interband matrix element of the electron momentum. The 2D exciton Bohr radius a_B^{2D} is given by $a_B^{2D} = \epsilon\hbar^2/4\mu e^2$ (μ is the exciton reduced mass).[13] From this equation one can see that the radiative lifetime is positively correlated with the dielectric constant, predicting longest radiative lifetime on HfO_2. However, the time-resolved PL spectra in Fig. 2(a) and (d) exhibited highly comparable radiative lifetimes for monolayer $MoSe_2$ on the three substrates, which means that Coulomb screening effect shows no obvious influence in our case.

Based on the discussion above, the dielectric screening effect from substrates has been

excluded as the dominating factor in determining the non-radiative exciton lifetime.

SUPPLEMENTARY NOTES 4: Theoretical simulation

The NAMD simulations were performed by Hefei-NAMD which augments the Vienna ab initio simulation package (VASP)[14-17] with the NAMD capabilities within TDDFT similar to Refs 18 and 19.[18,19] It has been successfully applied to photo-catalysis,[20] spin-polarized hole current,[21] electron-hole recombination[22] and van der Waals heterostructure interface.[23]

In the NAMD simulation, the time-dependent Kohn-Sham (TDKS) orbitals are expanded using a set of instantaneous adiabatic Kohn-Sham (KS) orbitals $\phi_i(\mathbf{r}, \mathbf{R}(t))$, which can be obtained by doing the static DFT calculations for each configuration $\boldsymbol{R}(t)$ along the adiabatic molecular dynamcis.

$$\Psi_e = \sum_j c_j(t)\phi_j(\mathbf{r}, \mathbf{R}(t)) \tag{1}$$

A set of differential equations for the coefficients can be obtained by inserting Eq. (1) into the TDKS equation:

$$i\hbar \frac{\partial}{\partial t} c_j(t) = \sum_k c_k(t) \left[\varepsilon_k \delta_{jk} - i\hbar \mathbf{d}_{jk}(t)\right], \tag{2}$$

where ε_k is the energy of the adiabatic state *k*, and $\mathbf{d}_{jk}$ is the non-adiabatic coupling (NAC) between the state *k* and *j* which is given by

$$\mathbf{d}_{jk} = \left\langle \phi_j \middle| \frac{\partial}{\partial t} \middle| \phi_k \right\rangle = \langle \phi_j | \nabla_{\mathbf{R}} | \phi_k \rangle \dot{\mathbf{R}} = \frac{\langle \phi_j | \nabla_{\mathbf{R}} H | \phi_k \rangle}{\varepsilon_k - \varepsilon_j} \dot{\mathbf{R}}. \tag{3}$$

The NACs are calculated in a finite difference method.[24,25] With the coefficients $c_j(t)$ and the NACs, hopping probabilities between the adiabatic KS states according to Tully's fewest-switches algorithm[26] can be obtained as:

$$\boldsymbol{P}_{j\to k}(t, \Delta t) = \frac{2\Re[c_j^* c_k \mathbf{d}_{jk}]\Delta t}{c_j^* c_j} \tag{4}$$

Further, the probabilities are multiplied by a Boltzmann factor within the classical path

approximation.[19,27,28] In this scheme the relaxation of the excited carriers is determined mainly by the NAC elements, in which the electron-phonon (*e-ph*) interaction is included.

We employed VASP to perform the static and ab initio molecular dynamics (AIMD) calculations. Electron−nuclei interactions were described by use of the projector-augmented wave pseudopotentials.[29,30] The Kohn-Sham wave functions were expanded in plane waves up to 400 eV and the convergence of the energies in the self-consistent step was achieved with a 10^{-4} eV threshold with Gaussian smearing method of 0.05 eV/Å. The calculations employed the Perdew-Burke-Ernzerhof (PBE) exchange-correlation functional.[31,32] The slab models were built with a vacuum region more than 15 Å in the Z direction in conjunction with the dipole correction[33] to avoid the fictitious interaction with its periodic images. After the geometry optimization, we used velocity rescaling to bring the temperature of the system to 300 K. A 5 ps microcanonical ab initio molecular dynamics trajectory was then generated with a time step of 1 fs. The conduction band minimum (CBM) is chosen as the initial state for electron relaxation. The NAMD results were based on average over 100 different initial configurations obtained from the MD trajectory. For each chosen structure, we sampled 2×104 trajectories for the last 3 ps. The phonon spectrum in Gamma point was performed with frozen phonon method which is implemented in VASP.[15-17] For HfO_2, Al_2O_3 and SiO_2, to match the lattice of $MoSe_2$, we chose the supercells as $HfO_2(010)(3\times3)||MoSe_2(001)(3\times2\sqrt{3})$, Al_2O_3 $(111)(2\times2)||MoSe_2(001)(3\times3)$ and SiO_2 $(111)(1\times1)||MoSe_2(001)(4\times4)$. The lattice mismatches are less than 5%. The interface models are shown in Supplementary Figure 9. Clean SiO_2 (111) surface is not stable.[34] It is easy to be saturated by hydrogen atoms or small molecules. Here we used hydrogen atoms to saturate the SiO_2 surface.[35]

Supplementary Reference:

1 Ceballos, F., Cui, Q., Bellus, M. Z. & Zhao, H. Exciton formation in monolayer transition metal dichalcogenides. *Nanoscale* **8**, 11681-11688, (2016).

2 Steinleitner, P. *et al.* Direct Observation of Ultrafast Exciton Formation in a Monolayer of WSe2. *Nano Lett.* **17**, 1455-1460, (2017).

3 Thilagam, A. Ultrafast exciton relaxation in monolayer transition metal dichalcogenides. *J. Appl. Phys.* **119**, 164306, (2016).

4 Selig, M. *et al.* Dark and bright exciton formation, thermalization, and photoluminescence in monolayer transition metal dichalcogenides. *2D Mater.* **5**, 035017, (2018).

5 Yu, Y. *et al.* Fundamental limits of exciton-exciton annihilation for light emission in transition metal dichalcogenide monolayers. *Phys. Rev. B* **93**, 201111 (2016).

6 Kumar, N. *et al.* Exciton-exciton annihilation in MoSe2monolayers. *Phys. Rev. B* **89**, 125427 (2014).

7 Sun, D. *et al.* Observation of rapid exciton-exciton annihilation in monolayer molybdenum disulfide. *Nano Lett.* **14**, 5625-5629, (2014).

8 Hoshi, Y. *et al.* Suppression of exciton-exciton annihilation in tungsten disulfide monolayers encapsulated by hexagonal boron nitrides. *Phys. Rev. B* **95**, 241403 (2017).

9 Ma, N. & Jena, D. Charge Scattering and Mobility in Atomically Thin Semiconductors. *Phys. Rev. X* **4**, 011043 (2014).

10 Jena, D. & Konar, A. Enhancement of carrier mobility in semiconductor nanostructures by dielectric engineering. *Phys. Rev. Lett.* **98**, 136805, (2007).

11 Lin, Y. *et al.* Dielectric screening of excitons and trions in single-layer MoS_2. *Nano Lett.* **14**, 5569-5576 (2014).

12 Raja, A. *et al.* Coulomb engineering of the bandgap and excitons in two-dimensional materials. *Nat. Commun.* **8**, 15251, (2017).

13 Robert, C. *et al.* Exciton radiative lifetime in transition metal dichalcogenide monolayers. *Phys. Rev. B* **93**, 205423, (2016).

14 Zhang, Y., Tan, Y.-W., Stormer, H. L. & Kim, P. Experimental observation of the quantum

Hall effect and Berry's phase in graphene. *Nature* **438**, 201 (2005).

15 Kresse, G. & Hafner, J. Ab initio molecular dynamics for liquid metals. *Phys. Rev. B* **47**, 558 (1993).

16 Kresse, G. & Hafner, J. Ab initio molecular dynamics for open-shell transition metals. *Phys. Rev. B* **48**, 13115 (1993).

17 Kresse, G. & Furthmüller, J. Efficient iterative schemes for ab initio total-energy calculations using a plane-wave basis set. *Phys. Rev. B* **54**, 11169 (1996).

18 Craig, C. F., Duncan, W. R. & Prezhdo, O. V. Trajectory surface hopping in the time-dependent Kohn-Sham approach for electron-nuclear dynamics. *Phys. Rev. Lett.* **95**, 163001 (2005).

19 Akimov, A. V. & Prezhdo, O. V. The PYXAID program for non-adiabatic molecular dynamics in condensed matter systems. *J. Chem. Theory Comput.* **9**, 4959-4972 (2013).

20 Chu, W. *et al.* Ultrafast Dynamics of Photongenerated Holes at a CH_3OH/TiO_2 Rutile Interface. *J. Am. Chem. Soc.* **138**, 13740-13749 (2016).

21 Zhao, C., Zheng, Q., Wu, J. & Zhao, J. Ab initio nonadiabatic molecular dynamics investigation on the dynamics of photogenerated spin hole current in Cu-doped MoS_2. *Phys. Rev. B* **96**, 134308 (2017).

22 Zhang, L. *et al.* Delocalized Impurity Phonon Induced Electron–Hole Recombination in Doped Semiconductors. *Nano Lett.* **18**, 1592-1599 (2018).

23 Zheng, Q. *et al.* Phonon-Assisted Ultrafast Charge Transfer at van der Waals Heterostructure Interface. *Nano Lett.* **17**, 6435-6442, (2017).

24 Billeter, S. R. & Curioni, A. Calculation of nonadiabatic couplings in density-functional theory. *J. Chem. Phys.* **122**, 034105 (2005).

25 Hammes‐Schiffer, S. & Tully, J. C. Proton transfer in solution: Molecular dynamics with quantum transitions. *J. Chem. Phys.* **101**, 4657-4667 (1994).

26 Tully, J. C. Molecular dynamics with electronic transitions. *J. Chem. Phys.* **93**, 1061-1071 (1990).

27 Wang, L., Akimov, A. & Prezhdo, O. V. Recent progress in surface hopping: 2011–2015. *J. Phys. Chem. Lett.* **7**, 2100-2112 (2016).

28 Long, R., Prezhdo, O. V. & Fang, W. Nonadiabatic charge dynamics in novel solar cell

materials. *Wiley Interdiscip. Rev.: Comput. Mol. Sci.* **7**, e1305 (2017).

29 Blöchl, P. E. Projector augmented-wave method. *Phys. Rev. B* **50**, 17953 (1994).

30 Kresse, G. & Joubert, D. From ultrasoft pseudopotentials to the projector augmented-wave method. *Phys. Rev. B* **59**, 1758 (1999).

31 Perdew, J. P., Burke, K. & Ernzerhof, M. Generalized gradient approximation made simple. *Phys. Rev. Lett.* **77**, 3865 (1996).

32 Perdew, J. P. *et al.* Atoms, molecules, solids, and surfaces: Applications of the generalized gradient approximation for exchange and correlation. *Phys. Rev. B* **46**, 6671 (1992).

33 Bengtsson, L. Dipole correction for surface supercell calculations. *Phys. Rev. B* **59**, 12301 (1999).

34 Malyi, O. I., Kulish, V. V. & Persson, C. In search of new reconstructions of (001) α-quartz surface: a first principles study. *RSC Adv.* **4**, 55599-55603 (2014).

35 Jiang, D. & Carter, E. A. First-principles study of the interfacial adhesion between SiO_2 and $MoSi_2$. *Phys. Rev. B* **72**, 165410 (2005).